Supplementary Information

Paperfuge: An ultra-low cost, hand-powered centrifuge inspired by the mechanics of a whirligig toy

M. Saad Bhamla[1], Brandon Benson[1]†, Chew Chai[1]†, Georgios Katsikis[2], Aanchal Johri[1], Manu Prakash[*1]

[1]Department of Bioengineering
[2]Department of Mechanical Engineering
Stanford University, Stanford, CA

† Equal contributions
[*]Corresponding author; E-mail: manup@stanford.edu

August 9, 2016

Contents

1 Supplementary Videos

1.1 S1: High-speed dynamics of paperfuge

Video of paperfuge ($R_{\text{d}} = 50$ mm) spun with hands recorded at 6000 frames per second. Application of force on the handles unwinds the strings, resulting in rotation of the central disc. The strings pass through a completely unwound state (parallel strings) and start to rewind, ultimately forming super-coiled structures.

1.2 S2: Measuring rotational speed (rpm)

Measuring the time-varying rotational speed (ϕ) of paperfuge ($R_{\text{d}} = 50$ mm) using image analysis.

1.3 S3: Twisting torque conditions

Video highlighting the different observations during the dynamics of a paperfuge, used for constructing an empirical function for the twisting torque ($\tau_{\text{Twist}}(\phi)$).

1.4 S4: Comparison of experiment and theory

Video comparing the experimental force (F) and rotational speed ϕ with our model. Experiments were conducted on a paperfuge with one end connected to a stationary force transducer, and the other connected to a handle (pulled by hand) mounted on a track to constrain the displacement in one axis.

1.5 S5: Separation of plasma from whole blood using paperfuge

Video showing step-by-step process to use the paperfuge as a centrifugation device, for conducting hematocrit analysis on human blood.

2 Supplementary Text

2.1 Buzzer Whirligig History

Gus W. Van Beek called the buzzer 'a universal toy through time and space' [34]. Archaeological excavations have revealed a large diversity of buzzer toys from ancient civilizations, from Indus valley to Native American cultures, across diverse time periods (Fig. 1 [A-H]). The geographical spread of these finds are global, with toys found in Israel, Lebanon, Greece, Egypt, Pakistan, India, USA, Brazil, Venezuela, Japan and China. In each of these places, the buzzer is called by onomatopoeic words that describe the sound the toy makes in local languages and dialects: whirligig, bull-roarer, buzz-bone, inyx, buzz, run-run, bum-bun, punggi-punggi, gurrifio, rumbador, furkalka, zun-zun, and zumbado. The oldest buzzer toys date back more than 5000 years to the Early Bronze Age (3300 BC) [34], making the buzzer toy an invention as old as the potter's wheel [35].

Disease	Parasite	Reference
Malaria	Plasmodium falciparum	[44, 45, 46, 47, 48]
West African tick-borne relapsing fever	Spirochetes	[49]
Bancroftian filariasis	Microfilaremia	[50, 51]
Leptospirosis	Leptospira	[52]
African trypanosomiasis	Trypanosoma brucei (T.b.) gambiense , T.b. rhodesiense	[53, 54]
Babesiosis	Babesia piroplasms	[55]
Pneumococcal disease	Pneumococcemia	[56]
American visceral leishmaniasis	Leishmania chagasi	[57]
Trichomonas,vaginalis infection	Trichomonas vaginalis	[58]

Table 1: List of human infectious diseases and their parasites that have been diagnosed succesfully using a QBC analysis.

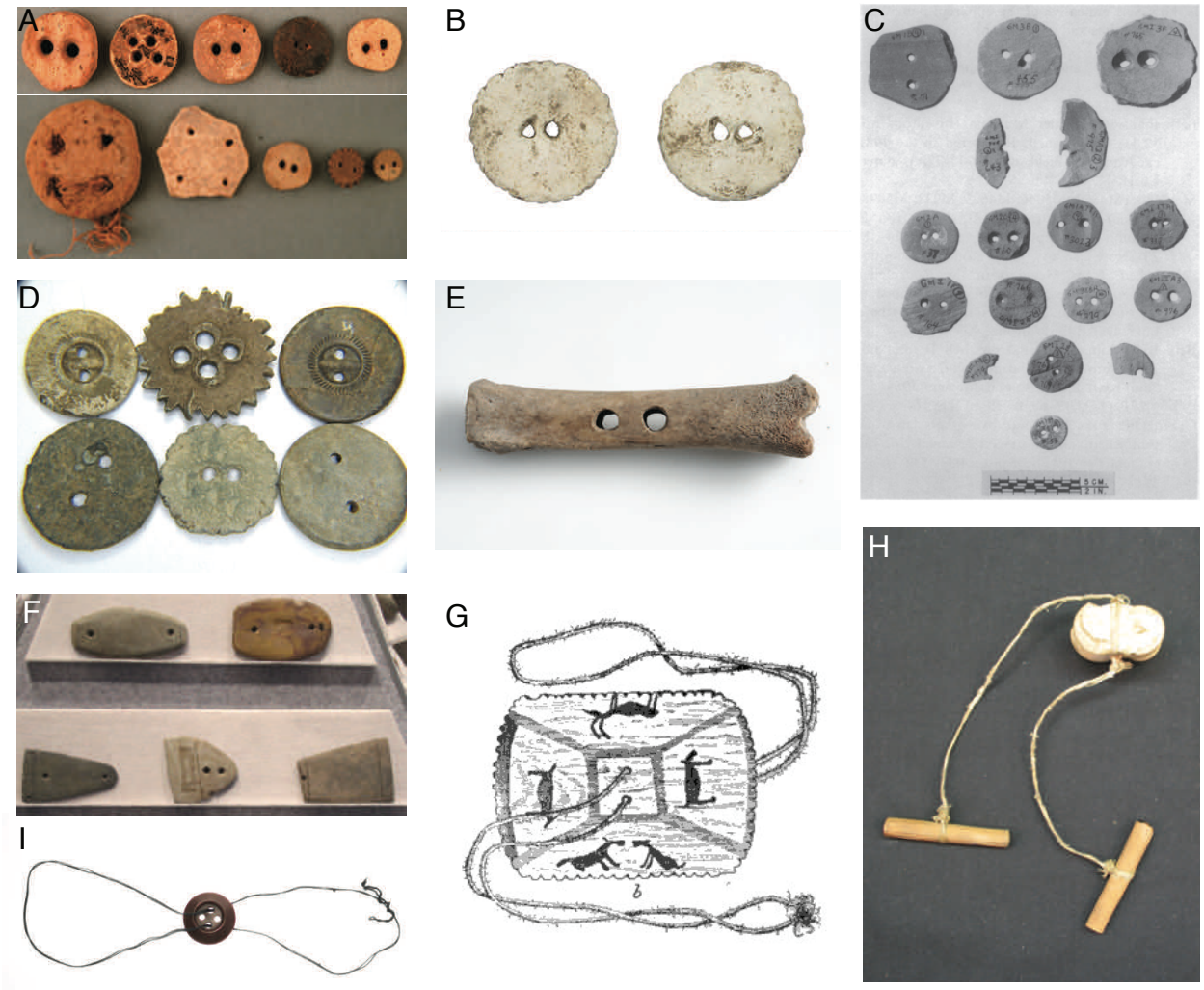

Figure 1: **Antique buzzer toys**. **A)** Pottery buzzers from Karanis, Egypt (2C-4C A.D.) Image from [36]. **B)** Lead alloy buzzer dating from the post-medieval period (1600-1800 A.D.). Image from [37]. **C)** Plate showing 17 Tell Jemmeh disks ranging from Late Bronze (1400-1200 B.C.) to Early Hellenistic (332-167 B.C.) ages. Image from [34]. **D)** Lead whirligigs with saw-tooth edges. Image from R. Dee and J. Winter [38]. **E)** Viking buzz-bone. Image source Swedish History Museum [39]. **F)** Stone Gorgets (buzz-buttons) from the Fource Maline Culture, a Native American culture from 300 BC-800 AD. Image source H. Rowe [40]. **G)** Eskimo buzz toy (1892). Image source [41]. **H)** A Caribou bone tied to a raw-hide, used as a charm. Image source [42]. **I)** A traditional button whirligig from Ukraine called 'furkalka'. Image from Enic [43].

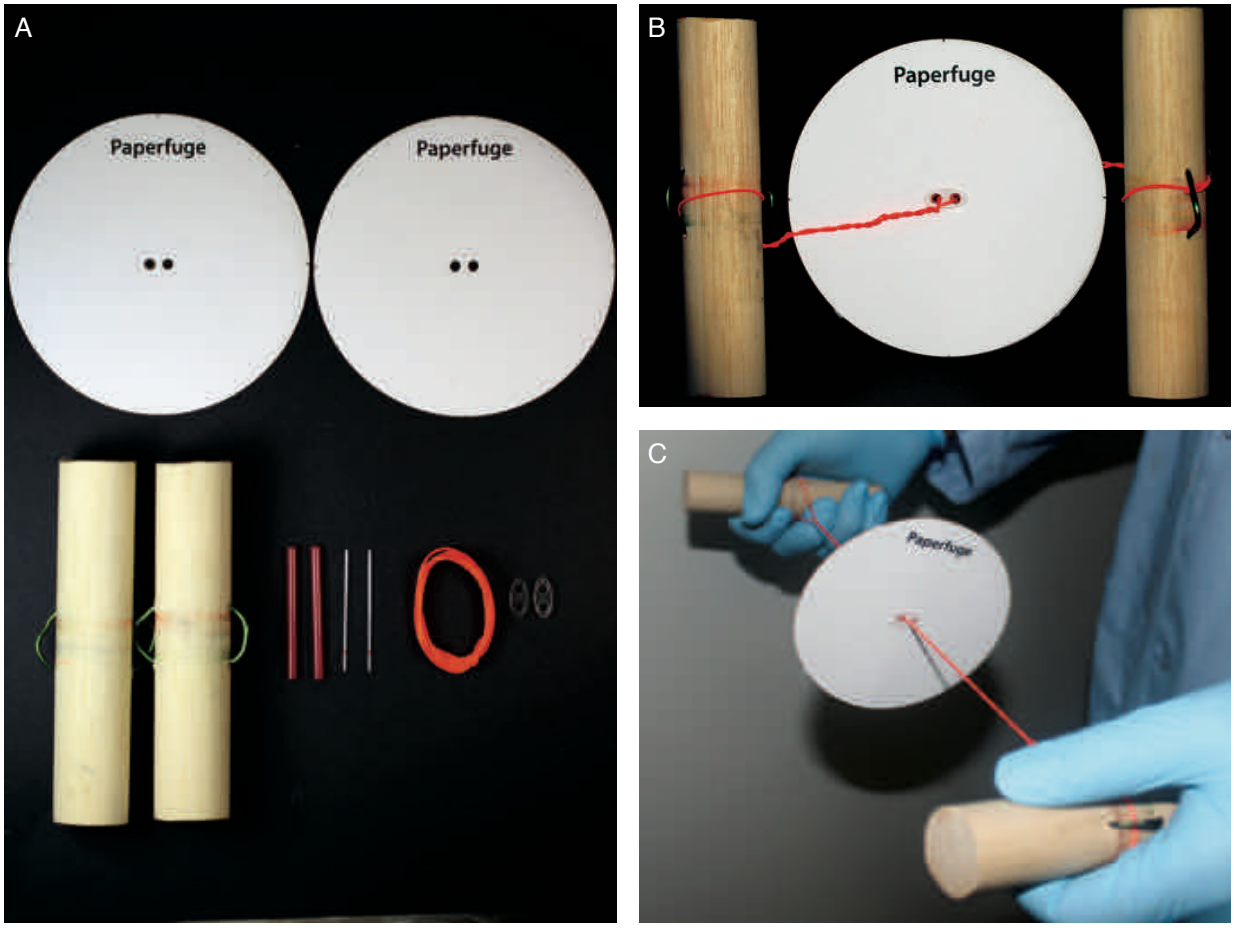

Figure 2: **Paperfuge Materials. A)** Materials used to construct a fully-functional paperfuge: paper-discs, wooden dowels (handles), string, capillaries, straws (capillary holders) and plastic shims. **B)** Constructed paperfuge showing flat form-factor, that easily fits in a pocket and can be carried in the field easily. **C)** To operate the paperfuge, the user utilizes the handles to gently and rhythmically pull on the strings.

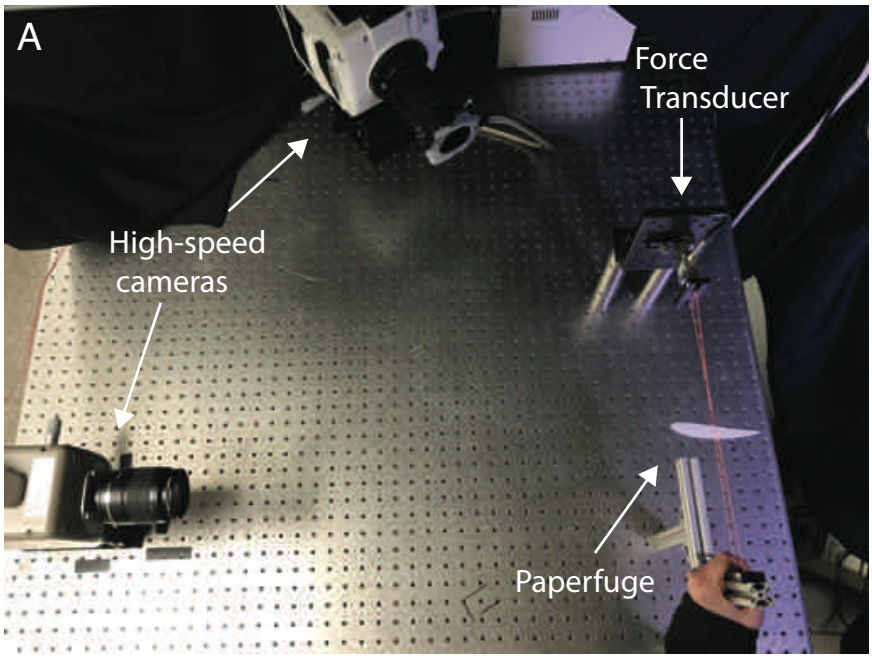

Figure 3: **High-Speed Setup** An experimental setup was constructed to measure the rotational speed, instantaneous force and string-coiling dynamics. A simple track was made to ensure that the hand-pulling movement was confined in one plane.

3 Supplementary Discussion: Theory Overview

We begin the paperfuge theoretical model, aiming to achieve predictive power over both frequency (f_0) and amplitude ($\dot{\phi}_{max}$) of the system. After correctly characterizing both amplitude and frequency of our oscillator, we will be able to explore the landscape of paperfuge parameters and input forces to optimize both the rotational speed ($\dot{\phi}$) and the corresponding relative centrifugal forces (RCF).

It is important to note that Schlichting and Suhr [59] take a step towards this goal in their paper, by proposing a model to describe the physical properties of the buzzer toy. Although they claim to have good agreement between experimental data and theory, their model lacks the predictive power that we seek over frequency and amplitude. The predictive power is crucial for creating scaling curves that characterize the scaling of $\dot{\phi}_{max}$ as a function of the system parameters such as R_d, R_s, L etc. The model presented by Schlichting and Suhr has two limitations: they drive the buzzer system at a known frequency, not allowing it to be determined by the system (system's resonant frequency), and they do not impose geometric constraints and boundary forces that naturally occur due to string coiling.

In this paper, we create a model for paperfuge that achieves this predictive power and harnesses it to optimize the paperfuge system. To do this, we tackle two sub-problems: 1. Achieve a high level of accuracy in our descriptive model (Section 3.1) 2. Generalize the input force (F) to create a predictive model (Section 3.6). In both sections, we continue to show the theoretical model results by comparing against experimental data, obtained using our high-speed setup.

3.1 Theoretical Model (Descriptive)

Modeling the paperfuge requires accounting for the main energies at play. We can identify the main energy components as:

- E_{Input} : energy of human input
- E_{Drag} : energy of air resisting motion
- E_{Twist} : energy of the string twisting and compressing, resisting motion
- E_{KE} : kinetic energy of the wheel

The human input serves as a source of energy while air drag and string twisting are dissipative in nature. Typically, energy is transferred from human input to kinetic energy of the wheel. It is then dissipated into air drag and string twisting energy, bringing the wheel to a stop. We begin by writing the Lagrangian for this system as:

$$\begin{aligned} L &= T - V \\ &= E_{\text{KE}}(\dot{\phi}) - \Big(E_{\text{Drag}}(\dot{\phi}) + E_{\text{Twist}}(\phi) + E_{\text{Input}}(\phi)\Big) \end{aligned} \tag{1}$$

We can differentiate both sides, to obtain the governing equation of motion as follows:

$$\frac{\partial}{\partial\phi}L = \frac{d}{dt}\frac{\partial}{\partial\dot{\phi}}L \tag{2}$$

$$-\frac{\partial}{\partial\phi}E_{\text{Twist}} - \frac{\partial}{\partial\phi}E_{\text{Input}} = \frac{d}{dt}\frac{\partial}{\partial\dot{\phi}}E_{\text{KE}} - \frac{d}{dt}\frac{\partial}{\partial\dot{\phi}}E_{\text{Drag}} \tag{3}$$

We can immediately substitute for kinetic energy $E_{KE} = \frac{1}{2}I\dot{\phi}^2$, and re-arrange to obtain:

$$I\ddot{\phi} = \frac{d}{dt}\frac{\partial}{\partial\dot{\phi}}E_{\text{Drag}} - \frac{\partial}{\partial\phi}E_{\text{Twist}} - \frac{\partial}{\partial\phi}E_{\text{Input}}. \tag{4}$$

We can re-write Eq. 4 in terms of the governing torques:

$$I\ddot{\phi} = \tau_{\text{Input}}(\phi) + \tau_{\text{Drag}}(\dot{\phi}) + \tau_{\text{Twist}}(\phi), \tag{5}$$

where I is the inertial moment of the disc, $\ddot{\phi}$ is the angular acceleration, and $\tau_{\text{Input}}, \tau_{\text{Drag}}, \tau_{\text{Twist}}$ are the input, air-drag and string-twisting contributions to the torque, respectively.

In the next few sections, we will define each of the torques based on the geometric parameters, as well as experimental observations.

We note that to create an accurate descriptive model, we explore different frictional assumptions (no-slip, slip and transition conditions) between the strings. We rigorously verify each assumption by comparing with experiments and establish the slip condition as the optimum choice for modeling the paperfuge.

The frictional assumptions that we explore pertain to how the string coils. In the extreme case where the surface of the string has no friction, the strings will slip against themselves until the twisting region achieves "uniform coiling". If some coiling region was more dense than another, the string would simply slip to alleviate this non-uniformity. We call this the "slip assumption" which we discuss in Section 3.2.1. In the other extreme, the strings would follow a no-slip condition where, once they touch, they do not slide against each other. We call this the "no-slip assumption" and discuss it in Section 3.2.2. Next we construct a method for transitioning between the two assumptions (Section 3.2.3). This transition is parameterized by a single variable. In Section 3.3, we use this variable along with video analysis to make a decision between the two frictional assumptions. We then discuss the twisting force in Section 3.4.

3.2 Input torque (τ_{Input})

A human hand provides a periodic input force to the system, $F(t)$. How is this translational force transferred to the rotational motion of the wheel?

We assume that the tension in the string is constant and that the string is massless and inextensible. With these two assumptions, a torque balance about the twisting region results in $\theta_h = \theta_w = \theta$, where θ is the angle from horizontal formed by the string at either the handle or the disc end as shown in Fig. 4A.

We begin by applying a torque balance on the disc by the strings. Only the force component in the plane of the disc ($T\sin\theta$) contributes to a torque (Fig. 4A). The $T\cos\theta$ component cancels out

due to symmetry. Since there are four strings connected to the wheel (two on either side), we can write the torque on the disc as:

$$\tau_{\text{Input}} = -\operatorname{sgn}(\phi) 4 R_s T \sin\theta, \tag{6}$$

where R_s is the radius of the string, T is the tension in the string and $\operatorname{sgn}(\phi)$ is the sign function defined as,

$$\operatorname{sgn}(\phi) = \begin{cases} 1 & \text{if } \phi > 0 \\ 0 & \text{if } \phi = 0 \\ -1 & \text{if } \phi < 0 \end{cases} \tag{7}$$

We can re-write T in terms of the applied force, F, as $2T\cos\theta = F$. We can, then, substitute for T in Eq. 6 to obtain:

$$\tau_{\text{Input}} = -\operatorname{sgn}(\phi) 2 R_s F \tan\theta. \tag{8}$$

To find $\tau_{\text{Input}}(\phi)$, we must find a relation between θ and ϕ. In the following sections, we apply the slip, no-slip, and transition conditions to find various relations between θ and ϕ.

3.2.1 Slip condition

In this slip condition, we allow the string to coil as if there is no friction. We will later show that this turns out to be the best assumption, as empirically we observe that the string twisting is relatively uniform in our experiments. Using geometry of the system, we can find the relationship between θ and ϕ. We divide the twisting section (L) into three parts (l_1, l_2, l_3) and can be seen in Fig. 4B. The first (l_1) and last (l_3) sections can be evaluated through simple geometry (Fig. 4B). The middle twisting region (l_2) can be understood as follows. We consider how a paper right triangle defined by internal angle θ can be wrapped around a pencil. We place the adjacent side against the pencil and begin rolling up the paper as in (Fig. 4B). The hypotenuse of the triangle creates a helix that serves as a proxy for the string. When the triangle is completely wrapped around the pencil, the opposite side of the triangle has the length ϕR_{pencil} where ϕ is the angle of rotation of the helix in radians and R_{pencil} is the radius of the pencil. We can also define the length of the string in the twist to be l_2. This results in the relation:

$$\sin\theta = \operatorname{sgn}(\phi)\frac{\phi R_{\text{pencil}}}{l_2}, \tag{9}$$

Applying this to the paperfuge, R_{pencil} becomes R_s, ϕ becomes the angle of rotation of the paperfuge disc, and θ is the angle subtended by the string as shown in Fig. 4B.

Because the three right triangles are similar, we can form one large right triangle that satisfies

$$\sin\theta = \frac{|\phi| R_s + R_h + R_w}{L}, \tag{10}$$

where R_h is the radius of the handle, and $2R_w$ is the distance between the two holes on the disc. This exercise provides us with a relation between θ and ϕ to evaluate τ_{Input} for the slip condition:

$$\tau_{\text{Input,slip}} = -\operatorname{sgn}(\phi) 2 R_s F \frac{|\phi| R_s + R_h + R_w}{\sqrt{L^2 - (|\phi| R_s + R_h + R_w)^2}} \tag{11}$$

We conduct a similar analysis for the no-slip condition next.

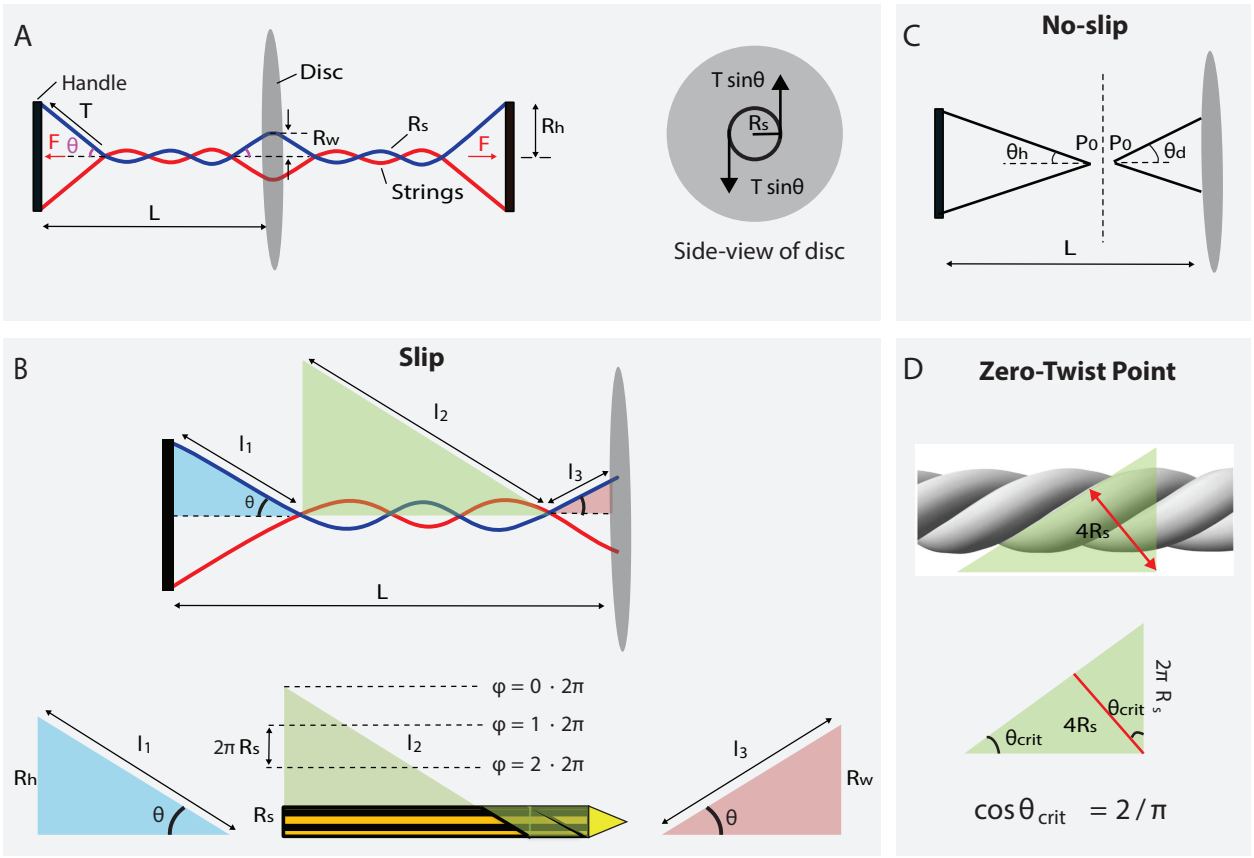

Figure 4: **Schematic for theoretical model. A)** Schematic illustrating the parameters for the paperfuge model. Side-view of the disc highlights the component of the string force creating a torque on the disc. **B) Slip condition:** For the slip assumption, to relate θ in terms of material parameters, we divide the total string (L) into three similar right triangles, corresponding to l_1, l_2, l_3. **C) No-slip condition:** Assuming high surface friction, the first point of contact during twisting becomes fixed at p_0. The two parts on either side of p_0 evolve independently. **D) Zero-twist point:** During twisting, the strings reach a critical point beyond which any further coiling is impossible without lateral compression or formation of secondary helical structures (super-coiling). By geometrical arguments, the corresponding θ_{crit} can be calculated for this point.

3.2.2 No-slip condition

In this no-slip condition, we assume that any point of contact between two strings remains fixed until the strings are separated. In other words, there is always enough friction between the strings so that they never slip against each other. This condition can be described as follows.

When ϕ is zero, the string is in an uncoiled state. As the strings start to twist (due to the rotation motion of the disc), their first point of contact is at point p_0, which is defined through geometrical constraints of the system (Fig. 4C). This creates two triangles defined by the angles θ_h and θ_d respectively. As the string begins to twist more, both angles increase and a twisting region grows outwards from p_0. During the whole cycle, the strings continue to touch at point p_0 adhering to the no-slip condition. Essentially this means that strings on the handle and disc sides evolve independently (Fig. 4C).

We now choose a reference frame that fixes p_0 so that the strings at this point do not rotate. In this reference frame, the disc and the handle rotate with an angular speed, $\dot{\theta_d}$ and $\dot{\theta_h}$, respectively. We also dissect the system at p_0, forming two separate systems defined by parameters: ϕ_i, θ_i, L_i, and R_i, where $i \in \{d, h\}$.

To characterize the evolution of the twisting region, we again utilize the pencil heuristic discussed in Section 3.2.1. First, we consider only an infinitesimally small change in ϕ, defined as $d\phi$. We imagine a correspondingly small triangle formed by unrolling the pencil and the large triangle formed by angle θ_d and the disc. Using the pencil heuristic, we can write the differential triangle as

$$\sin\theta = \mathrm{sgn}(\phi)\frac{d(\phi R_{\text{pencil}})}{dl_{\text{twist}_i}}, \tag{12}$$

where l_{twist} is the length of string between p_0 and the vertex of θ_i.

We replace the generic parameters with specific parameter of our system to yield:

$$\sin\theta_i = \mathrm{sgn}(\phi_i)\frac{d\phi_i R_s}{dl_{\text{twist}_i}}. \tag{13}$$

And for the larger triangle, we obtain the relation

$$\sin\theta_i = \frac{R_i}{L_i - l_{\text{twist}_i}}. \tag{14}$$

We now relate the handle and disc sides through their relative velocity, $\dot{\phi}$. We define positive rotation to be counter clock-wise about the axial axis, where the positive direction points from p_0 to the vertex of θ_i. Thus, both sides of the paperfuge are related through

$$\dot{\phi} = \dot{\phi_d} + \dot{\phi_h}. \tag{15}$$

As described earlier, due to the massless string assumption, we find that $\theta_h = \theta_w = \theta$. Using these relations, we can now integrate Eq. 13-15 to write an expression for the dependence of θ on the geometric parameters of the system, for a no-slip condition as:

$$\sin(\theta) = \frac{(R_h + R_w)e^{\kappa}}{L}, \tag{16}$$

where $\kappa = \frac{R_s|\phi|}{R_h+R_w}$. This enables us to solve for τ_{Input} for the no-slip condition:

$$\tau_{\text{Input,no-slip}} = -\operatorname{sgn}(\phi) 2R_s F \frac{(R_h + R_w)e^{\kappa}}{\sqrt{L^2 - ((R_h + R_w)e^{\kappa})^2}}. \tag{17}$$

3.2.3 Transition Condition

In this transition condition, we aim to find a general mathematical formalism that captures both the slip and no-slip asymptotic conditions through a single parameter. The advantage of such a formalism is two-fold: first, it enables a single-parameter model for seamlessly transitioning between the slip, no-slip boundary conditions, and second, it opens up the possibility of choosing a complex boundary condition, i.e., a transition boundary condition, which lies somewhere between slip and no-slip. As we will show, the slip condition is sufficient for our paperfuge data-sets; however, this exercise leaves us with a compact formalism that may serve useful to others.

We begin this transition by noting that for small ϕ, both models are the same. Using a first-order Taylor's series expansion on $\tau_{\text{Input,no-slip}}$ in Eq. 17 about $\frac{|\phi|R_s}{R_h+R_w}$ stated as:

$$e^{\frac{|\phi|R_s}{R_h+R_w}} \sim 1 + \frac{|\phi|R_s}{R_h + R_w}, \tag{18}$$

completely recovers the slip input torque ($\tau_{\text{Input,slip}}$), as shown in Eq. 11. Therefore, we now aim to create a continuous transition between the function e^{κ} and $1 + \kappa$ parametrized by a value, α, where $\kappa = \frac{|\phi|R_s}{R_h+R_w}$. One way to do this is through the following function:

$$\frac{e^{\alpha\kappa} + \alpha - 1}{\alpha}. \tag{19}$$

When $\alpha = 1$, we recover e^{κ}. We can also make α arbitrarily close to zero enabling us to expand $e^{\alpha\kappa}$ about α. Performing this expansion to first order gives

$$\frac{e^{\alpha\kappa} + \alpha - 1}{\alpha} \sim 1 + \kappa + O(\alpha^2), \tag{20}$$

which is our continuous transition between e^{κ} and $1 + \kappa$. Thus, the general equation for the input torque can now be re-written as follows:

$$\tau_{\text{Input,transition}} = -\operatorname{sgn}(\phi) 2R_s F \frac{(R_h + R_w)(\frac{e^{\alpha\kappa}+\alpha-1}{\alpha})}{\sqrt{L^2 - ((R_h + R_w)(\frac{e^{\alpha\kappa}+\alpha-1}{\alpha}))^2}}, \tag{21}$$

where $\alpha \in (0, 1]$ with $\alpha = 0$ and $\alpha = 1$ recovers $\tau_{\text{Input,slip}}$ and $\tau_{\text{Input,no-slip}}$, respectively. We will demonstrate in Section 3.3 that the slip condition ($\alpha = 0$) matches remarkably well with our experimental data-sets. However, α allows for the abstraction of frictional conditions which may be useful to other researchers utilizing our model for different string twisting systems.

3.3 Drag torque (τ_{Drag})

We now tackle the second major force acting on the paperfuge: air drag. When a disc revolves in a fluid at angular velocity $\dot{\phi}$, a boundary layer develops around the disc. We assume that the

Reynolds number of this system is high ($Re \sim 10^5$), resulting in an air resistance force proportional to velocity squared and the surface area of the disc. We also assume that the wheel has a cylindrical shape. We leave the radius and width of this cylinder as free parameters, R_d and w_d. Over a small surface with area, dS_d, and velocity, $V = R_\mathrm{d}\dot{\phi}$, we posit that force of air resistance, F_Drag, is

$$F_{Drag} = -a_R S_\mathrm{d} \left(R_\mathrm{d}\dot{\phi}\right)^2. \tag{22}$$

where a_R is the drag coefficient that depends on the fluid properties (air density and viscosity), as well as the surface frictional properties of the paper-disc. The parameter a_R has to be obtained empirically, by matching experiments and theory. For a small surface element S_d on the wheel of the paperfuge, V becomes a function of radius along the wheel. Integrating over the surface of a wheel with radius, R_d, and width, w_d, results in the following expression for the torque,

$$\tau_\mathrm{Drag} = -a_R \,\mathrm{sgn}(\dot{\phi}) \left(\frac{4\pi}{5} R_\mathrm{d}^5 + 2\pi w_d R_\mathrm{d}^4\right) \dot{\phi}^2. \tag{23}$$

At this point we have two degrees of freedom in our system: a_R and α. Soon we will introduce another degree of freedom, γ, due to τ_Twist (Section 3.4). To simplify the decision between frictional conditions, we exclude τ_Twist in comparing experiments to theory to obtain the empirical values for a_R and α. We justify this as follows. τ_Drag and τ_Twist dominate during different parts of the oscillation cycle, allowing removal of τ_Twist without interfering with τ_Drag.

In Fig. 5A, we compare experimental data of a paperfuge ($R_\mathrm{d} = 50$ mm) with the theoretical model with $\alpha = 0$, $\alpha = 1$ and $\alpha = 0.6$, corresponding to slip, no-slip and transition conditions, respectively. We observe that slip-model captures the experimental data, both qualitatively and quantitatively well, for $a_R = 0.003$. Furthermore, we confirm the slip boundary condition by showing a periodic distribution of twists across the length of the string, as shown in Fig. 5B.

3.4 Twisting torque (τ_Twist)

We now construct a term that accounts for many forces in the paperfuge dynamics associated with the string. As the paperfuge winds up, it reaches a geometric maximum that it can only pass by forming supercoiling structures. To account for this geometric maximum, supercoiling, and other possible parameters such as coiling resistance, string elasticity, string surface friction, we define an empirical equation, with a single-free parameter (γ).

To construct this formulation, we write down three specific boundary conditions, corresponding to how the string undergoes twisting, as shown in Fig. 6A. We will then construct a continuous function that satisfies all three boundary conditions, ultimately resulting in a single-parameter formulation for $\tau_\mathrm{Twist}(\phi)$. The parameter γ will be obtained by comparing the theoretical model with experimental data.

We present the three observations, which are illustrated in Fig. 6A(i-iii), as follows:

(i) At $\phi = 0$, we do not expect any torque on the disc, i.e., $\boldsymbol{\tau}_\mathrm{Twist}(\boldsymbol{\phi})\big|_{\boldsymbol{\phi=0}} = \mathbf{0}$.

(ii) When $\theta = \theta_\mathrm{crit}$, string in the twisting region lays against itself. This gives us an opportunity to characterize the stiffness of the string as it compresses, resulting in braking force to the paperfuge wheel. We approximate the torque at this point with a linear spring force model: $\frac{\boldsymbol{\partial}}{\boldsymbol{\partial\phi}}\boldsymbol{\tau}_\mathrm{Twist}(\boldsymbol{\phi})\big|_{\boldsymbol{\phi=\phi}_\mathrm{crit}} = \boldsymbol{k}$, where k is the spring constant.

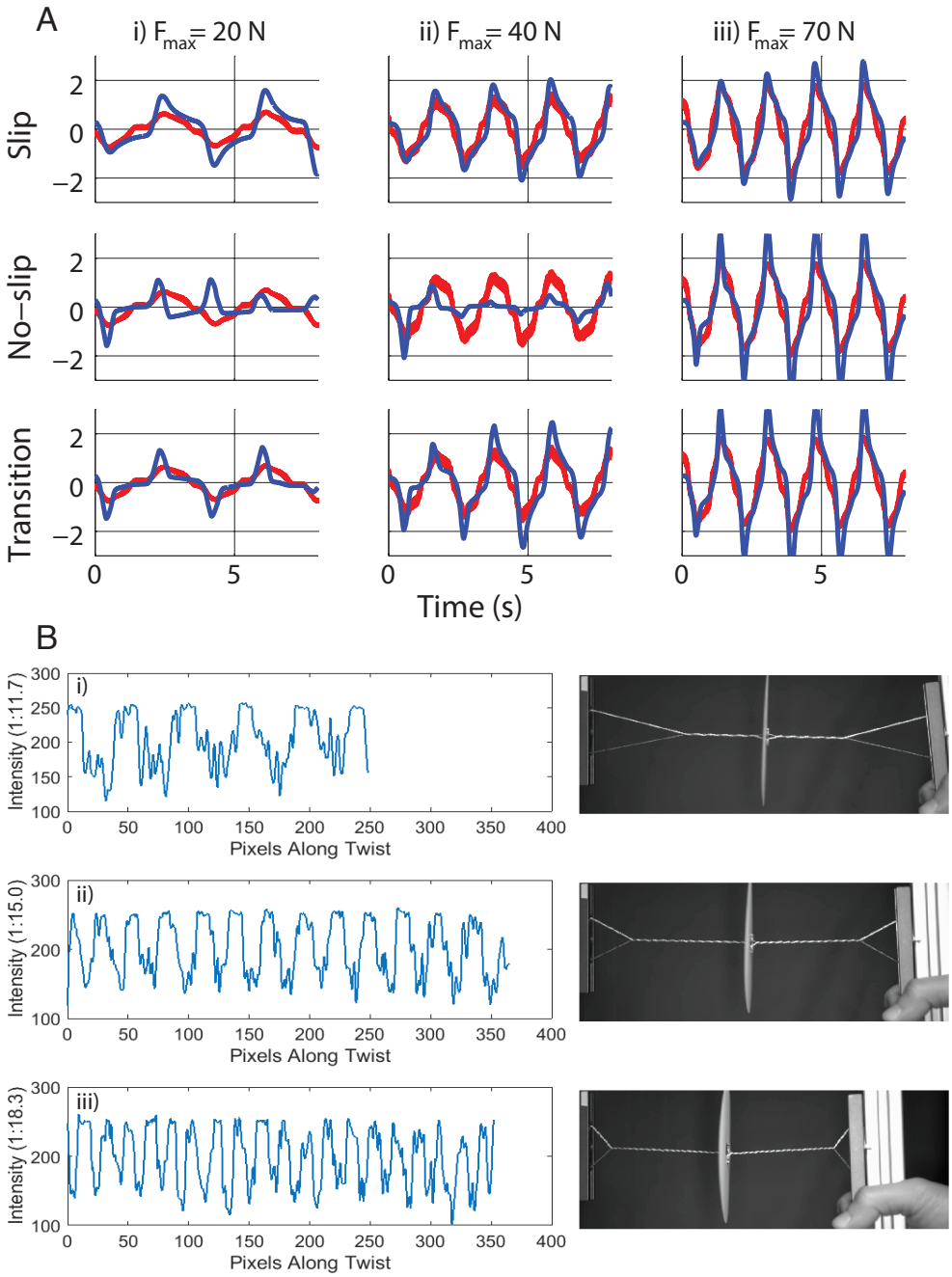

Figure 5: **Evaluating slip, no-slip and transition boundary conditions. A)** Comparison of experimental data with theory reveals $a_R = 0.003$ as an optimal value for the frictional parameter across all boundary conditions (slip $\alpha = 0$, no-slip $\alpha = 1$ and transition $\alpha = 0.6$). We find that the slip assumption has the most reliable fit to the data, confirmed by experimental observations. **B)** Plots of pixel intensity across the twisting region (right side of disc) at three different times points (i-iii) during coiling. The periodicity of pixel intensity peaks reflects the uniform spacing of twists, confirming that the slip condition is indeed the most accurate description of our experiments (see video S3).

(iii) ϕ cannot exceed some maximum value, $\phi_{\max}$ (defined below), which is decided by the geometry of the system. This yields: $\boldsymbol{\tau_{\text{Twist}}(\phi)\big|_{\phi=\phi_{\max}} = \infty}$.

For the simplicity of our model, we assume $k = 1$; however we introduce a free-parameter, γ, below that we use to tune our system.

To obtain a continuous function satisfying the above three conditions, we use a function of the form $\tau_{\text{Twist}}(\phi) = -\operatorname{sgn}(\phi) A \left[\frac{1}{(B-|\phi|)^{\gamma}} - C\right]$, where γ is a free parameter and A, B, C are found using the three constraints discussed above.

$$A = \frac{1}{\gamma}(\phi_{\max} - \phi_{\text{crit}})^{\gamma+1} \tag{24}$$

$$B = \phi_{\max} \tag{25}$$

$$C = \phi_{\max}^{-\gamma}. \tag{26}$$

Substituting these parameters, we can re-write the expression for $\tau_{\text{Twist}}(\phi)$ as:

$$\tau_{\text{Twist}}(\phi) = -\operatorname{sgn}(\phi)\frac{1}{\gamma}(\phi_{\max} - \phi_{\text{crit}})^{\gamma+1}\left[\frac{1}{(\phi_{\max} - |\phi|)^{\gamma}} - \frac{1}{\phi_{\max}^{\gamma}}\right]. \tag{27}$$

We now need to define ϕ_{crit} and $\phi_{\max}$. To calculate ϕ_{crit}, it is easier to calculate θ_{crit}, which is illustrated in Fig. 4D. This is the zero-twist point where the string cannot twist any further without undergoing compression or forming super-coiling structures [60], and is defined as $\cos\theta_{\text{crit}} = 2/\pi$. Using Eq. 10, we can then calculate ϕ_{crit}.

Now, to find the value of $\phi_{\max}$, we imagine that the twisting region spans the distance from the disc to the handle. This means that in Fig. 4B, only the green triangle is present (l_2). Additionally, we know that θ_{crit} defines this triangle. Thus, using Eq. 9, we can obtain $\phi_{\max}$ as:

$$\sin\theta_{\text{crit}} = \frac{|\phi_{\max}|R_s}{L - (R_h + R_w)} \tag{28}$$

Finally, we now evaluate Eq. 27 for different values of γ as shown in Fig. 6B.

At this point, we have defined all the terms in Eq. 5 and by substituting all the torque terms, we can re-write the governing equation of motion for the paperfuge as follows:

$$\begin{aligned} I\ddot{\phi} = &-\operatorname{sgn}(\phi) 2R_s F \frac{|\phi|R_s + R_h + R_w}{\sqrt{L^2 - (|\phi|R_s + R_h + R_w)^2}} - a_R \operatorname{sgn}(\dot{\phi})\left(\frac{4\pi}{5}R_{\text{d}}^5 + 2\pi w_d R_{\text{d}}^4\right)\dot{\phi}^2 \\ &- \operatorname{sgn}(\phi)\frac{1}{\gamma}(\phi_{\max} - \phi_{\text{crit}})^{\gamma+1}\left[\frac{1}{(\phi_{\max} - |\phi|)^{\gamma}} - \frac{1}{\phi_{\max}^{\gamma}}\right]. \end{aligned} \tag{29}$$

We compute Eq 29 numerically, and validate with experimental data at different forces for a single disc ($R_{\text{d}} = 50$ mm). We estimate a value of $\gamma = 6$ that works best for our paperfuge system (Fig 6B).

Even though we can solve this non-linear equation numerically to compare with the experimental data, it is complex and non-intuitive. In the next section, we show how this equation can be reduced to a linear form to guide our intuition.

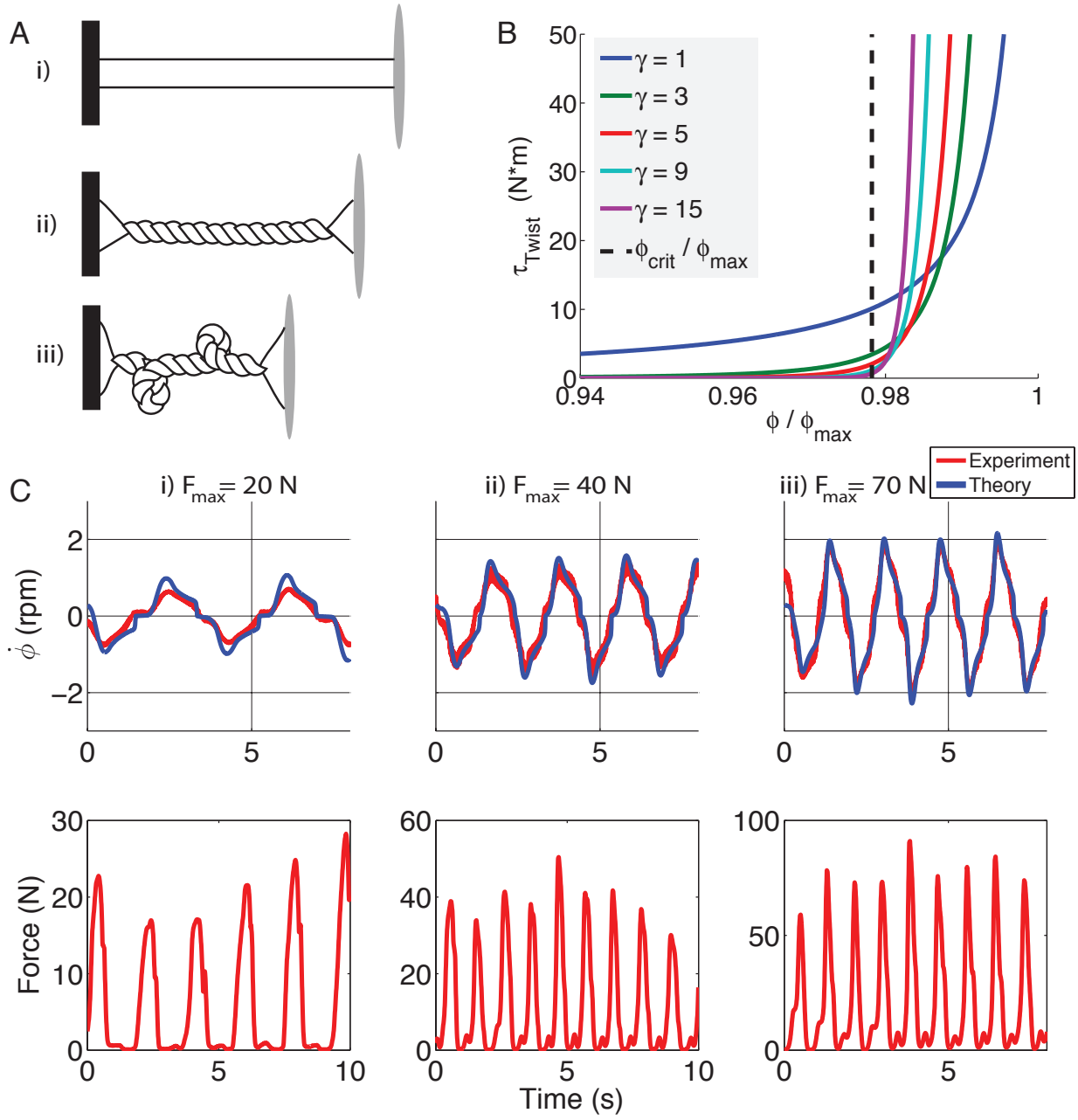

Figure 6: **Twisting Torque. A)** Schematic illustrating the governing conditions for the τ_{Twist}: i) $\tau_{\text{Twist}}(\phi)\big|_{\phi=0} = 0$, ii) $\tau_{\text{Twist}}(\phi)\big|_{\phi=\phi_{\max}} = \infty$, and iii) $\frac{\partial}{\partial\phi}\tau_{\text{Twist}}(\phi)\big|_{\phi=\phi_{\text{crit}}} = 1$. **B)** Characterization of τ_{Twist} for different values of the parameter γ. **C)** Choosing $\gamma = 6$ and utilizing experimental force into the model, we show that our theory accurately describes a $R_{\text{d}} = 50$ mm paperfuge across input forces with different peak-amplitudes of $F_{\max} = 20,\ 40$, and 70 N.

3.5 Gaining Intuition: Simple Harmonic Oscillator (SHO)

By reducing Eq. 29 to a simple harmonic oscillator, we can intuitively understand how frequency (f_0) and rotational velocity ($\dot{\phi}$) scale with changes in system parameters.

As discussed above, there are three major forces at play in our paperfuge system: input, drag force and string-twisting force. To simplify our model, we keep the input force constant and neglect the latter two forces. We justify this as follows: 1) The air drag force is dissipative and dampens the motion of the system (neglecting the drag force will not affect the scaling trends). 2) The twisting force is also a dissipative force that acts mainly when the string has over-twisted ($\phi > \phi_{\text{crit}}$ from the zero-twist geometric constraint in Section 3.4). Therefore we can neglect the twisting force if we enforce $\phi \leq \phi_{\text{crit}}$.

Eq. 29 can now be simplified to:

$$I\ddot{\phi} = -\operatorname{sgn}(\phi) 2FR_s \tan\theta \tag{30}$$

We make one final approximation. We assume that the blue and red triangles are much smaller than the green triangle (the twisting region as previously shown in Fig. 4B), which means that $R_h \sim R_w \sim 0$. Now we can write the simplified expression:

$$\tan\theta = \frac{\phi R_s}{\sqrt{L^2 + (\phi R_s)^2}} \tag{31}$$

$$\sim \frac{\phi R_s}{L}. \tag{32}$$

Substituting this into Eq. 30 gives:

$$I\ddot{\phi} = -\frac{2FR_s^2}{L}\phi, \tag{33}$$

which is a SHO of the form $\ddot{x} = -\omega^2 x$, where $\omega = \sqrt{\frac{2F_m R_s^2}{IL}}$ is the angular frequency of the system and F_m is a constant corresponding to the peak-amplitude of the input force.

Since for a paperfuge (centrifuge), we care about the maximum RPM and RCF, we can write both these terms simply as:

$$\dot{\phi}_{\text{max}} = \phi_{\text{crit}}\omega \tag{34}$$

$$= \frac{L\sqrt{\pi^2 - 2^2}}{2R_s}\sqrt{\frac{2F_m R_s^2}{IL}} \tag{35}$$

$$\propto \sqrt{\frac{LF_m}{I}} \tag{36}$$

$$RCF = \frac{R_{\text{d}} < \dot{\phi}^2(t) >}{g} \tag{37}$$

$$= \frac{R_{\text{d}}\dot{\phi}_{\text{max}}^2}{2g} \tag{38}$$

We can validate this scaling intuition by comparing with the scaling analysis found in Section 3.7, in which we use the model to numerically scale the system parameters. For our disc with constant density ρ, we have $I = \frac{\pi}{2}\rho w_d R_d^4$. This results in $\omega \propto \frac{1}{R_d^2}$, $\dot{\phi}_{\max} \propto \frac{1}{R_d^2}$, $\omega \propto \frac{1}{\sqrt{w_d}}$, and $\dot{\phi}_{\max} \propto \frac{1}{\sqrt{w_d}}$. We indeed capture these trends as shown Fig. 8A,B. As we increase radius (R_d) and width (w_d) of the disc respectively, which ultimately increases I. Furthermore, $\omega \propto R_s$ while $\phi_{\max}$ has no dependence, as defined above. Indeed, in Fig. 8C, we show that frequency shows a linear dependence on R_s and $\phi_{\max}$ is relatively constant. Likewise, scaling L yields $\omega \propto \frac{1}{\sqrt{L}}$ and $\phi_{\max} \propto \sqrt{L}$ which we see accurately depicted in Fig. 8D.

3.6 Making Model Predictive: A Theoretical Input Force

We begin modeling the input force of a human (F) by finding a paperfuge parameter that highly correlates with the input force. Upon inspection, we identify θ to be the optimum parameter to scale F. θ varies between fixed values from 0 to 90 degrees, and is therefore, less affected by changes in parameters such as string length (L), disc radius (R_d), and string radius (R_s). Experience of handling the paperfuge re-affirms this choice: by playing with paperfuge, we realize as users that our largest cue to begin pulling on the paperfuge is when it winds up all the way and needs to be unwound. This happens when θ becomes large. Thus, we can always use θ as a cue for us to begin pulling regardless of other changes to the system geometry.

We show that forces with varying peak-amplitudes ($F_{\max} =$ 20, 40, and 70 N) show similar cyclical profiles as a function of θ in Fig. 7(A,B). Here the paperfuge cycle traverses the curve in the counter-clockwise direction, where $F_{\max}$ occurs during an unwinding phase as the user applies a force to set the paperfuge disc spinning in motion. We use this as a reference to construct a theoretical input force, $F_{\mathrm{th}}(\theta)$. As seen in Fig. 7C, there are three major regions in the F_{th} vs. θ space. The first region is when $\theta < \theta_{\text{min-start}}$. Using both experimental $F(\theta)$ data-sets (Fig. 7A,B) and by tuning to achieve good agreement, we set $\theta_{\text{min-start}} = 35°$. Experimentally, this corresponds to the region when the disc is winding up due to its inertial mass, and the user is applying negligible force.

The second region is defined when $\theta > \theta_{\text{min-start}}$. During this phase, the force takes on some small value, $F_{\min}$, which serves to slow the disc. We define the value of $F_{min} = 0.2F_{\max}$, based on experimental observations, where $F_{\max}$ is the maximum amplitude of the applied force. Both the first and second regions correspond to the wind up phase. The last region is during unwinding of the strings, where the angle θ decreases. During this phase, the user pulls the hardest to accelerate the paperfuge and unwind the strings. In this region, we define the force as a linearly decreasing function, between $F_{\max}$ and $F_{\max}/2$. Using this approach, we have a simple protocol to generate different theoretical input force profiles, $F_{\mathrm{th}}(\theta)$. To validate our approach, we create a phase-space plot showing good agreement between our theoretically generated dynamics and experimental data for $R_\mathrm{d} = 50$ mm (Fig. 7D).

3.7 Scaling Analysis

The values of the parameters employed during the scaling analysis are listed in Table 2.

We explore how the disc radius (Fig. 8A) and width (Fig. 8B) affect the maximum rotational velocity ($\dot{\phi}_{\max}$) and frequency (f_0). We find that both $\dot{\phi}_{\max}$ and f_0 decrease drastically as we increase the

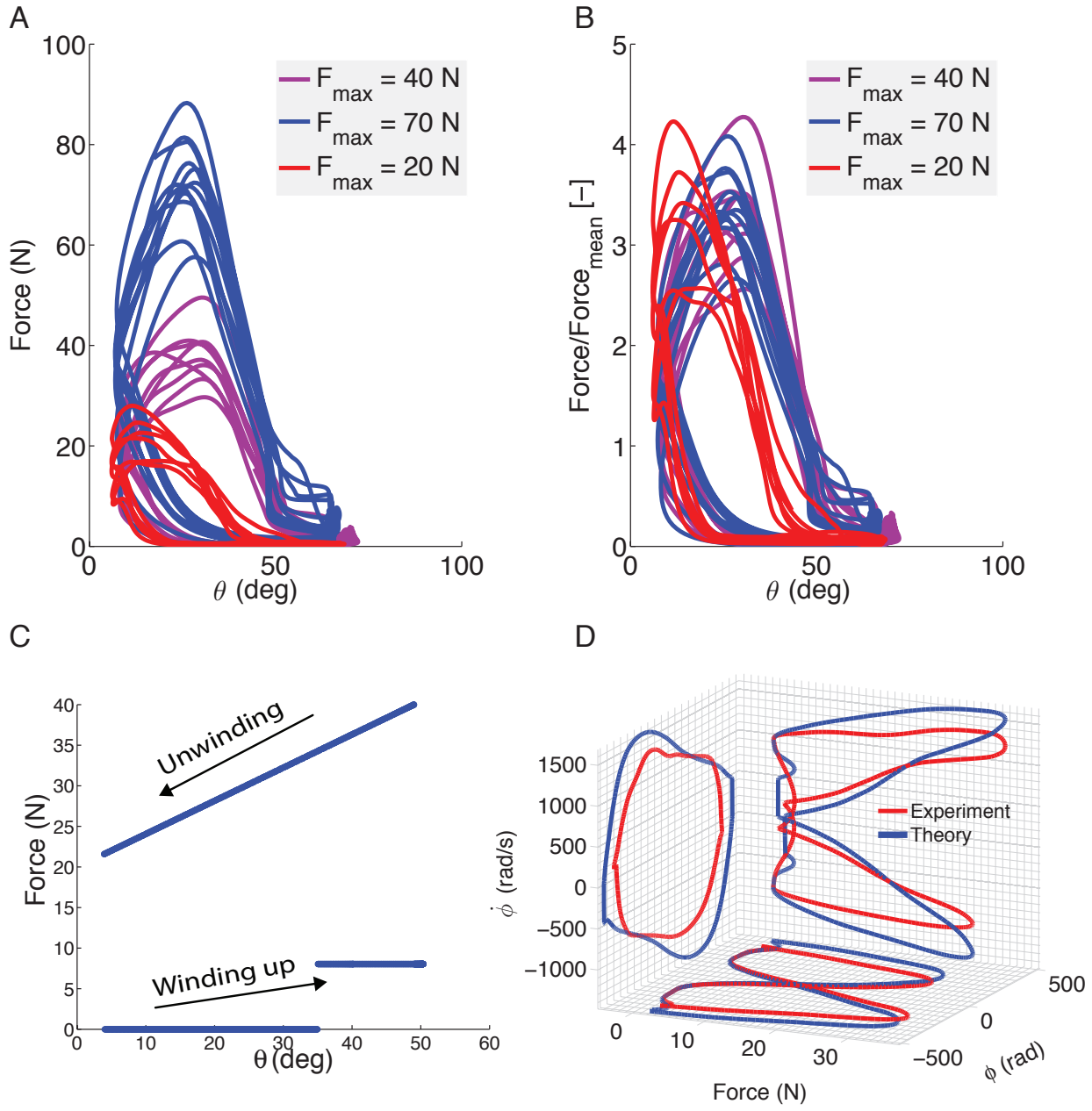

Figure 7: **Theoretical Input Force. A)** Experimental force vs. θ at varying force-amplitudes ($F_{\max} =$ 20, 40, and 70 N) for $R_{\mathrm{d}} = 50$ mm. **B)** Normalized Experimental force vs. θ space reveal that the force profiles collapse onto each other. **C)** Theoretical input force $F_{\mathrm{th}}(\theta)$ profile constructed from A and B. **D)** Phase space spanned by $\dot{\phi}$, F, and ϕ, highlighting excellent agreement between theory and experiment.

Parameters	Values
a_R (kg m^{-3})	0.003
k (N m)	1
γ [−]	6
ρ (kg m^{-3})	1000
R_w (mm)	0.3
R_h (mm)	11
$\theta_{\text{min-start}}$	35

Table 2: Parameter values used in scaling analysis

radius and width of the disc, which in turn, increases the moment of inertia ($I = \frac{\pi}{2}\rho w_d R_d^4$) and the drag force.

Next, we show how changes in string radius (Fig. 8C) and length (Fig. 8D) affect the maximum rotational velocity ($\dot{\phi}_{\max}$) and frequency (f_0). As discussed in Section 3.7, increasing the string radius results in a linear increase in frequency while $\dot{\phi}_{\max}$ remains constant. Based on Eq. 29, an increase in R_s causes a larger input torque. However, due to increased geometric constraints, the disc has less time to accelerate. These two effects balance each other, resulting in a relatively constant $\dot{\phi}_{\max}$. In contrast, increasing the string length increases $\dot{\phi}_{\max}$ and decreases f_0. More specifically, $\phi_{\max}$ is affected, allowing the input forces to be applied for longer, thus the disc accelerates for a longer time.

Disc Radius (R_d)	5 mm	12.5 mm	25 mm	50 mm	85 mm
Maximum Input Force (N)	3	18	27	40	50
Disc width (mm)	1.2	4.5	1.2	0.3	0.3
Mass (g)	0.26	2.6	2.2	2.4	6.5
Total String Length (m)	0.91	0.69	0.66	0.66	0.99
String Radius (mm)	0.05	0.25	0.25	0.25	0.50

Table 3: Experimental parameters for various sizes of paperfuge

3.8 Calculating Effective RCF

We discuss and compare two methods for finding an effective RCF. The first reduces the varying $\dot{\phi}(t)$ to a constant value through a time average. This results in

$$\text{Effective RCF} = \frac{R_{\text{d}}\langle\dot{\phi}^2(t)\rangle}{g}, \tag{39}$$

where $[\dot{\phi}] = \text{rad/s}$.

The second method for finding effective RCF involves accounting for the entire shape of $\dot{\phi}(t)$. We can solve for the time it takes for paperfuge to separate plasma and blood cells. We then identify our effective RCF by finding a constant $\dot{\phi}_{\text{effective}}$ such that it separates plasma and blood cells in the same amount of time as $\dot{\phi}(t)$.

To validate our first method and compare that to our second one, we employ the particle sedimentation model derived by Wong et al. [61], and plot the volume of plasma obtained as a function of

time of centrifugation (Fig. 9B). By using $\dot{\phi}^2_{\text{constant}}$ attained through time average, we find that our calculated V_{constant} (red) matches $V(t)$ (blue) very closely. We find here that though the maximum $\dot{\phi}$ of 50 mm paperfuge is $\sim$ 22000 rpm, the effective $\dot{\phi}$ is $\sim$ 13000 rpm. This means that spinning the paperfuge at $\dot{\phi}_{\text{max}}$ of 22000 rpm is equivalent to operating a traditional centrifuge at 13000 rpm.

Both methods are validated because of their clear agreement. We also note that the periodic nature of paperfuge can be seen in the plot of $V(t)$. As the paperfuge stops during its rotation cycle, we expect that the sedimentation pauses and $V(t)$ is approximately constant. As paperfuge re-starts, we expect to see the slope of $V(t)$ to become larger. Indeed, we observe these periodic changes in Fig. 9B.

Finally, by choosing equivalent design parameters, we show a theoretical surface plot that describes the RCF dependence on disc radius and input force with overlayed experimental data (in red circles, Fig. 9A). We also provide a table of parameters of various paperfuge sizes (Table 3) that we tested (Fig. 9C) along with the $\dot{\phi}_{\text{max}}$ and effective RCF we attain using these devices (Fig. 9D).

Parameter	Symbol
Force input	F
String radius	R_s
Handle radius	R_h
Disc radius	R_{d}
Acrylic oval radius	R_w
String length	L
Angular displacement	ϕ
Angular velocity	$\dot{\phi}$
Frequency of the disc	f_0
Disc density	ρ
Air drag constant	a_R
Disc width	w_d
Spring constant	k
Moment of inertia	I
Angle between string and handle	θ
Hyperparameter	γ
Kinetic Energy	E_{KE}
Input Energy	E_{Input}
Drag Energy	E_{Drag}
Twisting Energy	E_{Twist}

Table 4: List of parameters used in the theoretical model.

References

[34] van Beek, G. W. The Buzz: A Simple Toy from Antiquity. *Bulletin of the American Schools of Oriental Research* 53 (1989). URL http://www.jstor.org/stable/1356880?origin=crossref.

[35] Anthony, D. W. *The Horse, the Wheel, and Language.* How Bronze-Age Riders from the Eurasian Steppes Shaped the Modern World (Princeton University Press, Prince-

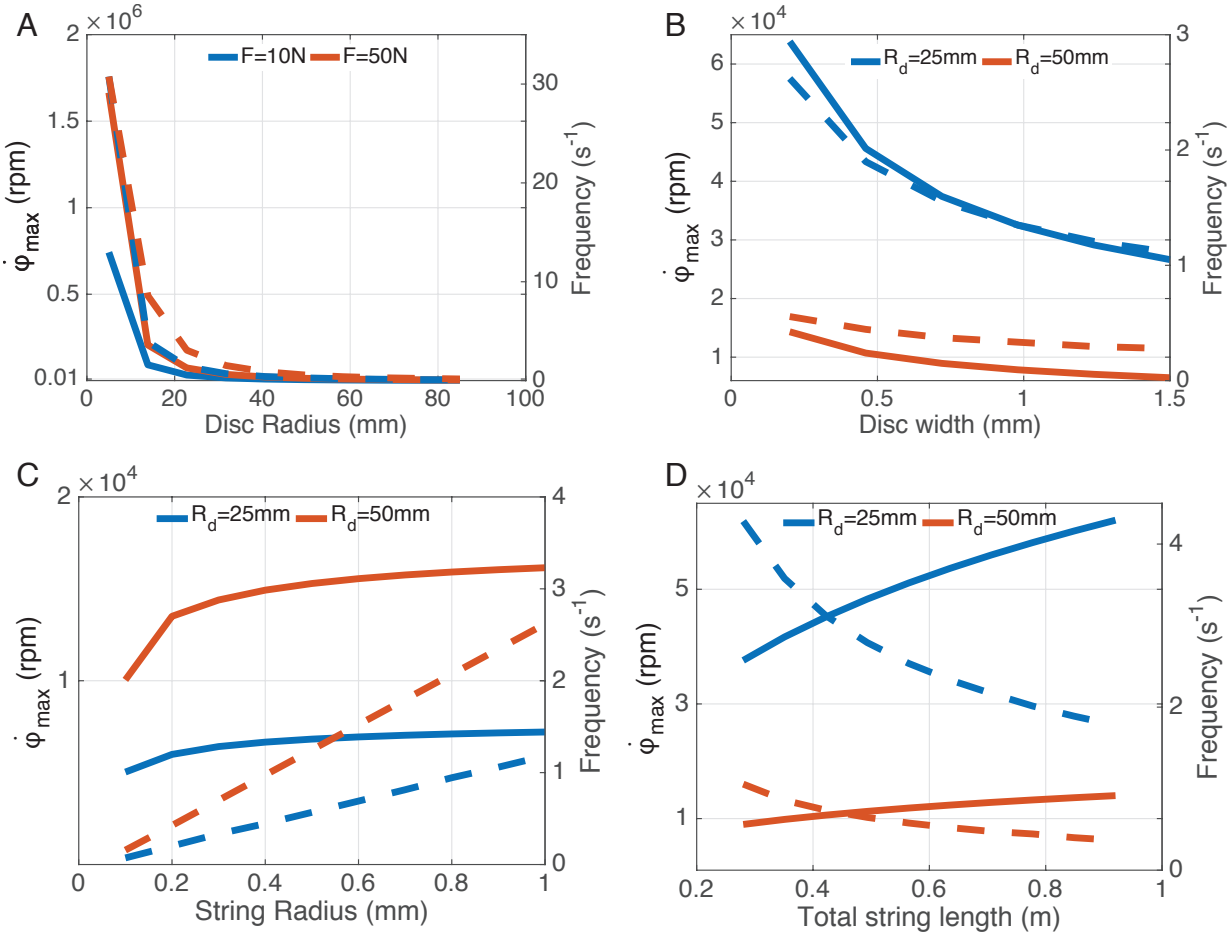

Figure 8: **Theoretical design landscape for paperfuge scaling.** The output variables of the paperfuge, maximum rotational speed $\dot{\phi}_{\max}$ (shown in solid-lines) and frequency f_0 (shown in dashed-lines) depend non-linearly on the system parameters. In each plot, unspecified parameters default to the following: $R_d = 50$ mm, $w_d = 0.3$ mm, $R_s = 0.25$ mm, $4L = 0.661$ m and $F = 40$ N. **A)** $[\dot{\phi}_{\max}, f_0] = f(R_{\mathrm{d}}, F)$: Decreasing the size of disc dramatically increases the rpm (exceeding million rpm), with a concomitant increase in frequency - the higher frequencies are only theoretically achievable, but not humanly possible, due to fundamental anatomic constraints. **B)** $[\dot{\phi}_{\max}, f_0] = f(w_d, R_{\mathrm{d}})$: Increasing the width of the disc contributes to the overall inertial mass, resulting in lower speeds as well as lower frequencies. **C)** $[\dot{\phi}_{\max}, f_0] = f(R_s, F)$: Increasing the string radius leads to an increase in the torque transmitted to the disc, and thus results in higher $\dot{\phi}_{\max}$, which ultimately plateaus due to geometric constraints of constant L. **D)** $[\dot{\phi}_{\max}, f_0] = f(L, R_d)$: For smaller discs, $\dot{\phi}_{\max}$ increases with increasing string length, however frequency f_0 decreases (longer string takes more time to twist, thus increasing the intervals between twist-untwist regions.

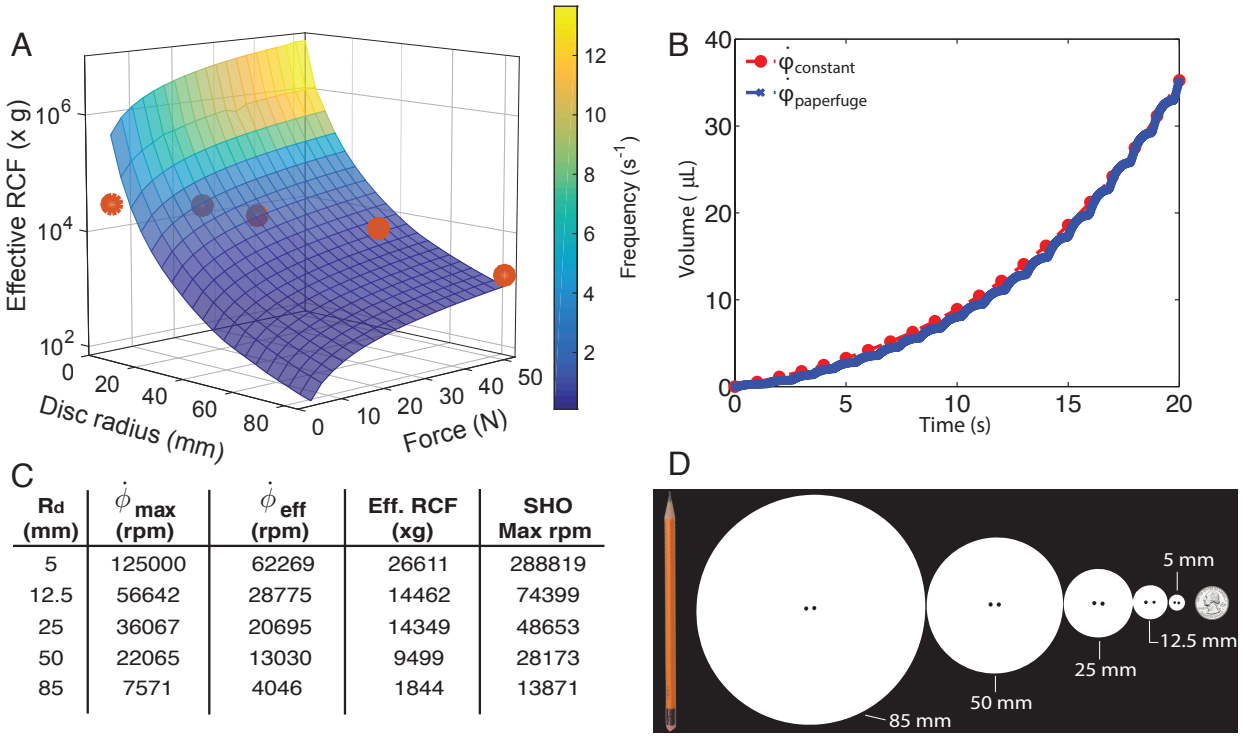

Rd (mm)	$\dot{\phi}_{max}$ (rpm)	$\dot{\phi}_{eff}$ (rpm)	Eff. RCF (xg)	SHO Max rpm
5	125000	62269	26611	288819
12.5	56642	28775	14462	74399
25	36067	20695	14349	48653
50	22065	13030	9499	28173
85	7571	4046	1844	13871

Figure 9: **Scaling of RCF for paperfuge. A)** Scaling curve of disc radius and input force for desirable effective RCF with experimental data in red. To generate this curve, the parameters used are: $w_d = 0.3$ mm, $4L = 0.661$ m. The values for R_s were interpolated between 0.05 mm to 0.50 mm to correspond to experimental parameters (Table 3) **B)** Validation curve for effective RCF calculation. **C)** Maximum speed ($\dot{\phi}_{\max}$), Effective speed ($\dot{\phi}_{\text{eff}}$), and Effective RCF attained experimentally from different paperfuges. $\dot{\phi}_{\max}$ attained from SHO approximation is also provided for comparison. **D)** Images of various sized paperfuges used in this study, with a pencil and a U.S. quarter shown for scale.

ton, 2010). URL http://www.degruyter.com/view/books/9781400831104/9781400831104/9781400831104.xml.

[36] Pottery toy buzzers. URL http://courseweb.stthomas.edu/jmjoncas/LiturgicalStudiesInternetLinks/EgyptianNonChristianWorship/EgyptianWorshipMusic/AncientEgyptianMusic.html.

[37] Lead buzzer. URL https://finds.org.uk/database/artefacts/record/id/718419.

[38] Lead whirligig. URL http://www.johnwinter.net/jw/2014/07/the-lead-whirligig/.

[39] Viking buzz bone. URL https://www.flickr.com/photos/historiska/13618876824/in/set-72157643391922024/.

[40] Stone Buzzer Fourche Maline Culture. URL https://en.wikipedia.org/wiki/Fourche_Maline_culture#/media/File:Fourche_Maline_Gorgets_HRoe_2010.jpg.

[41] N, W. W., Powell, J. J. W., Murdoch, J. & Bourke, J. G. Ninth Annual Report of the Bureau of Ethnology to the Secretary of the Smithsonian Institution, 1887-88. *The Journal of American Folklore* **7**, 80 (1894). URL http://www.jstor.org/stable/532969?origin=crossref.

[42] Caribou bone twirling buzzer. URL http://www.tipatshimuna.ca/1110_f.php?catalogue_no=III-B-8.

[43] Button whirligig. URL https://en.wikipedia.org/wiki/Whirligig.

[44] Adeoye, G. O. & Nga, I. C. Comparison of Quantitative Buffy Coat technique (QBC) with Giemsa-stained thick film (GTF) for diagnosis of malaria. *Parasitology International* **56**, 308–312 (2007). URL http://linkinghub.elsevier.com/retrieve/pii/S1383576907000943.

[45] Pinto, M. J., Rodrigues, S. R., Desouza, R. & Verenkar, M. P. Usefulness of quantitative buffy coat blood parasite detection system in diagnosis of malaria. *Indian journal of medical microbiology* **19**, 219–221 (2001). URL http://eutils.ncbi.nlm.nih.gov/entrez/eutils/elink.fcgi?dbfrom=pubmed&id=17664839&retmode=ref&cmd=prlinks.

[46] Benito, A., Roche, J., Molina, R., Amela, C. & Alvar, J. Application and evaluation of QBC malaria diagnosis in a holoendemic area. *Applied parasitology* **35**, 266–272 (1994). URL http://eutils.ncbi.nlm.nih.gov/entrez/eutils/elink.fcgi?dbfrom=pubmed&id=7812314&retmode=ref&cmd=prlinks.

[47] Baird, J. K., Purnomo & Jones, T. R. Diagnosis of malaria in the field by fluorescence microscopy of QBC® capillary tubes. *Transactions of The Royal Society of Tropical Medicine and Hygiene* **86**, 3–5 (1992). URL http://trstmh.oxfordjournals.org/cgi/doi/10.1016/0035-9203(92)90412-6.

[48] Spielman, A. *et al.* Malaria diagnosis by direct observation of centrifuged samples of blood. *American Journal of Tropical Medicine and Hygiene* **39**, 337–342 (1988). URL http://eutils.ncbi.nlm.nih.gov/entrez/eutils/elink.fcgi?dbfrom=pubmed&id=3189696&retmode=ref&cmd=prlinks.

[49] van Dam, A. P., van Gool, T., Wetsteyn, J. C. & Dankert, J. Tick-borne relapsing fever imported from West Africa: diagnosis by quantitative buffy coat analysis and in vitro culture of Borrelia crocidurae. *Journal of Clinical Microbiology* **37**, 2027–2030 (1999). URL http://jcm.asm.org.ezproxy.stanford.edu/content/37/6/2027.full.

[50] Bawden, M., Slaten, D. & Malone, J. QBC®: rapid filaria diagnoses from blood—Mansonella ozzardi and Wuchereria bancrofti. *Transactions of The Royal Society of Tropical Medicine and Hygiene* **88**, 66–66 (1994). URL http://trstmh.oxfordjournals.org/cgi/doi/10.1016/0035-9203(94)90503-7.

[51] Freedman, D. O. & Berry, R. S. Rapid diagnosis of Bancroftian filariasis by acridine orange staining of centrifuged parasites. *American Journal of Tropical Medicine and Hygiene* **47**, 787–793 (1992). URL http://eutils.ncbi.nlm.nih.gov/entrez/eutils/elink.fcgi?dbfrom=pubmed&id=1281967&retmode=ref&cmd=prlinks.

[52] Kramer, K. J., Pang, L. W. & Minette, H. P. Evaluation of the quantitative buffy coat analysis (QBC) system for the detection of Leptospira in human blood. *Southeast Asian journal ...* (1994). URL http://www.tm.mahidol.ac.th/seameo/1994-25-4/1994-25-4-788.pdf.

[53] Bailey, J. W. & Smith, D. H. The quantitative buffy coat for the diagnosis of trypanosomes. *Tropical doctor* (1994). URL http://tdo.sagepub.com/content/24/2/54.short.

[54] Levine, R. A., Wardlaw, S. C. & Patton, C. L. Detection of haematoparasites using quantitative buffy coat analysis tubes. *Parasitology Today* **5**, 132–134 (1989). URL http://linkinghub.elsevier.com/retrieve/pii/0169475889900562.

[55] Mattia, A. R., Waldron, M. A. & Sierra, L. S. Use of the Quantitative Buffy Coat system for detection of parasitemia in patients with babesiosis. *Journal of Clinical Microbiology* **31**, 2816–2818 (1993). URL http://jcm.asm.org.ezproxy.stanford.edu/content/31/10/2816.abstract.

[56] Wever, P. C. *et al.* Detection of pneumococcemia by quantitative buffy coat analysis. *European journal of clinical microbiology & infectious diseases : official publication of the European Society of Clinical Microbiology* **22**, 450–452 (2003). URL http://eutils.ncbi.nlm.nih.gov/entrez/eutils/elink.fcgi?dbfrom=pubmed&id=12827533&retmode=ref&cmd=prlinks.

[57] Liarte, D. B. *et al.* QBC for the diagnosis of human and canine american visceral leishmaniasis: preliminary data. *Revista da Sociedade Brasileira de Medicina Tropical* **34**, 577–581 (2001). URL http://eutils.ncbi.nlm.nih.gov/entrez/eutils/elink.fcgi?dbfrom=pubmed&id=11813066&retmode=ref&cmd=prlinks.

[58] Hammouda, N. A., Hegazy, I. H. & Tawfik, T. A. A rapid diagnostic test for Trichomonas vaginalis infection. *Journal of the Egyptian Society of Parasitology* **27**, 341–347 (1997). URL http://eutils.ncbi.nlm.nih.gov/entrez/eutils/elink.fcgi?dbfrom=pubmed&id=9257972&retmode=ref&cmd=prlinks.

[59] Schlichting, H. J. & Suhr, W. The buzzer—a novel physical perspective on a classical toy. *European Journal of Physics* **31**, 501–510 (2010). URL http://iopscience.iop.org/article/10.1088/0143-0807/31/3/007.

[60] Bohr, J. & Olsen, K. The ancient art of laying rope. *EPL (Europhysics Letters)* **93**, 60004 (2011). URL http://iopscience.iop.org.ezproxy.stanford.edu/0295-5075/93/6/60004/fulltext/.

[61] Wong, A. P., Gupta, M., Shevkoplyas, S. S. & Whitesides, G. M. Egg beater as centrifuge: isolating human blood plasma from whole blood in resource-poor settings. *Lab on a Chip - Miniaturisation for Chemistry and Biology* **8**, 2032–2037 (2008). URL http://pubs.rsc.org/en/content/articlehtml/2008/lc/b809830c.